

MSE Master Thesis

Blanket Cooling of a Fusion Reactor

Robert Beaufait

robertpeter.beaufait@hslu.ch; +41 41 349 31 84

Technikumstrasse 21, 6048 Horw, Switzerland

Advisor:

Prof. Dr. Ludger Fischer, Co-Leader CC Thermal Energy Storage

ludger.fischer@hslu.ch; +41 41 349 35 33

Technikumstrasse 21, 6048 Horw, Switzerland

Industry/Business Partner:

Caroline Sorensen, Commonwealth Fusion Systems/MIT

csorensen@cfs.energy

148 Sidney Street, Cambridge, MA 02139, USA

Expert:

Dr. Gianfranco Guidati, Energy Science Center, ETH Zürich

gianfranco.guidati@esc.ethz.ch

SOIC C 1, Sonneggstrasse 28, 8006 Zürich, Switzerland

Abstract

The use of digital tools for design is becoming a more common approach to engineering solutions. In many instances it is more cost effective than iterating laboratory measurement set-ups through estimation and trial and error. Numerical simulation software when properly applied helps to constrain the field of consideration by focusing resources on a starting point closer to the solution. However, numerically simulated physics is neither exact and results must be validated either by available theory and/or empirical measurement. This thesis utilizes numerical simulations with COMSOL Multiphysics and compares them with experimental measurements for a high-power heat exchanger. The development of the simulation and experimental set-up are described, and an outlook is offered based on results and observations. Future development is given by the author and CFS as recommendation for the continued research of this technology and its applications.

Table of Contents

Declaration of authorship	i
Abstract.....	ii
Table of Contents.....	iii
List of Figures	iv
List of Tables	v
Nomenclature	vi
Acronyms	vii
1 Introduction.....	1
1.1 Project background	1
1.2 Project aim and objectives.....	1
2 Materials and methods	1
2.1 Design and construction.....	2
2.2 Simulation and experiment.....	4
2.3 Simulation and experimental comparison	7
3 Results and discussion	9
3.1 Simulation vs. experimental set-up	9
4 Conclusion and future development	14
4.1 Conclusion.....	14
4.2 Future development.....	14
Appendix A.....	15
5 References	33

List of Figures

Figure 1: Schematic of experimental test rig.....	2
Figure 2: Exploded view of design concept.....	3
Figure 3: Working principles of the experimental test rig.....	4
Figure 4: Simulation domain.	5
Figure 5: Experimental test rig.	5
Figure 6: Heat flux temperature sensors and heating elements (a); Outlet temperature sensors (a) and (b).....	6
Figure 7: Inlet temperature sensor.	6
Figure 8: Diaphragm pump (a); Oval-wheel flow meter (b); Transmitter/controller (c).	7
Figure 9: Average wall temperature estimation.	8
Figure 10: Absolute difference of the average inlet and outlet temperatures between simulation and measurements.....	9
Figure 11: Relative difference between simulation and experiment for average inlet and outlet temperatures.	10
Figure 12: Fluid heat transfer coefficients.....	12
Figure 13: Bubble on inlet temperature sensor.....	13
Figure 14: Outgassing of air from tap water.....	13

List of Tables

Table 1: Equipment and materials used in construction of experimental set-up.	2
Table 2: Flow rates and power levels evaluated.	7
Table 3: Summary of quantities compared.	9
Table 4: Calculated heat flows into analyzed channels for simulations and experiments.....	10
Table 5: Specific heat flux densities for simulations and experiments.....	11
Table 6: Fluid heat transfer coefficient result for each compared case.	12

Nomenclature

quantity	description	unit
P	heating power	[W]
T	temperature	[°C]
x	position	[m]
λ	thermal conductivity	[W/(m·K)]
\dot{q}''	specific heat flux	[W/m²]
\dot{m}	mass flow rate	[kg/s]
\dot{Q}	heat flow	[W]
A	central channel area	[m²]
α	fluid heat transfer coefficient	[W/(m²·K)]
\dot{V}	flow rate	[l/min]
dw	distance to wall	[m]
dx	distance between points	[m]

Acronyms

name	description
CAD	Computer-aided Design
CCTES	Competence Center Thermal Energy Storage
CFS	Commonwealth Fusion Systems
FLiBe	Lithium-Fluoride-Beryllium salt
HSLU	Lucerne University of Applied Sciences and Arts
HTF	Heat Transfer Fluid
MAN DWE	Maschinenfabrik Augsburg-Nürnberg Energy Solutions AG
ORNL	Oak Ridge National Laboratory
PEXS	Power Exhaust System
PTFE	Polytetrafluorethylen

1 Introduction

1.1 Project background

The Competency Center Thermal Energy Storage (CCTES) is conducting a research study in cooperation with the industry partner Commonwealth Fusion Systems (CFS) to develop a concept for a part of the power exhaust system (PEXS) necessary for the removal of heat from a fusion reactor core. The reactor core consists of the fusion fuels reacting in a magnetically confined vacuum vessel requiring cooling. Vacuum vessel heat flux density reaches a peak of 12 MW/m^2 which needs to be removed via FLiBe (Fluoride-Lithium-Beryllium) molten salt to maintain material integrity [1]. Initial numerical simulations found (appendix A) it is within model error that the boundary conditions are met. However, no data exists to validate the model and its output which is the focus of this thesis.

1.2 Project aim and objectives

An earlier investigation (Appendix A) confirmed it was feasible to construct millimeter-scale channels in a flat plate to transfer enough heat to satisfy the boundary conditions [1]. This was discovered using an unvalidated numerical simulation. Further iteration with numerical tools requires validation through comparison with empirical measurements. This phase of the project was the construction of an experimental test rig to collect measurements and compare them with a numerical model. External industry experts in the field were consulted for guidance and/or expertise in using the materials proposed in Appendix A. The results were collected and analyzed to determine the accuracy of the simulated results with experimental measurements. Conclusions and future development recommendations are offered as this an active area of research and development within the fusion reactor design community.

2 Materials and methods

The validation of a numerical simulation requires a representative data set for comparison. It entails a design where boundary conditions are similar within a digital and physical environment. Attempts were made to incorporate materials which closely resembled the material properties of tungsten and FLiBe for the experimental set-up. Informative requests and meetings with CFS [2], Hyme [3], Seaborg [4], MAN DWE® [5], and ORNL [6,7] revealed equipment for this application does not exist, or is in the beginning of a conceptual phase. Therefore, the means to construct and validate the numerical simulation would have to come by using common materials at temperature and power levels achieved with off-the-shelf equipment.

2.1 Design and construction

The PEXS was designed to be both simulated numerically and built as an experimental test rig. A combination of geometry, machineability, and feasibility had to be considered before running simulations and conducting measurements. The boundary conditions stated by CFS [1] prove to be too cumbersome, expensive, and hazardous for an in-house experimental set-up. A concept was developed using readily available materials for the construction of the heat exchanger and for the heat transfer fluid. Figure 1 below shows a schematic of the proposed experimental test rig.

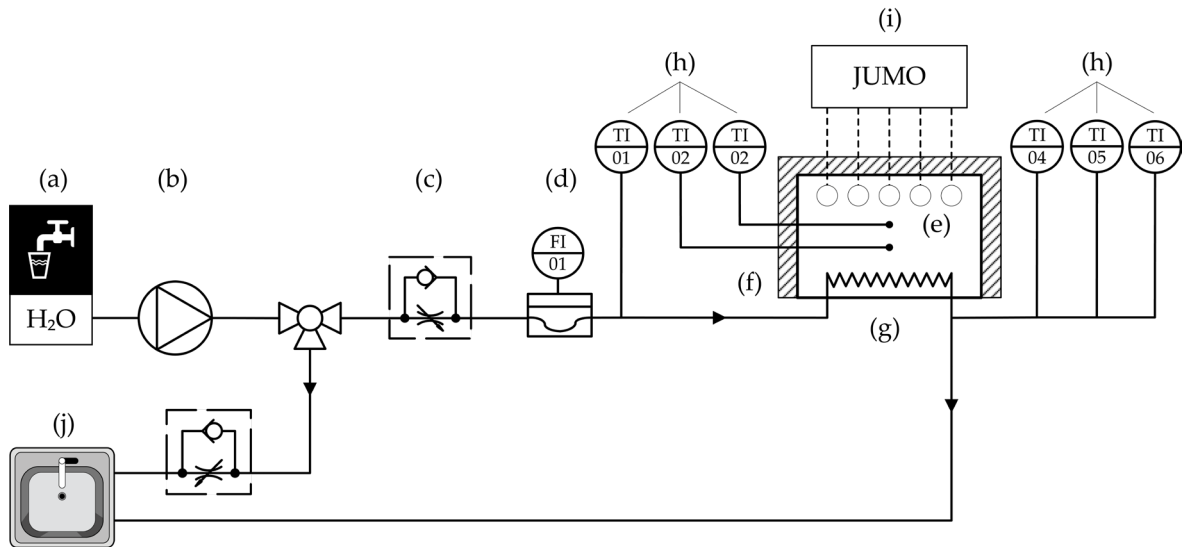


Figure 1: Schematic of experimental test rig.

Cool tap water (10-15°C) from the HSLU laboratory (a) was pumped (b) through a regulating valve (c), a volume flow indicator (d), through a heated (e) insulated (f) copper heat exchanger (g), past temperature sensors (h) recording inlet and outlet temperatures on a JUMO data logger (i), and discharging heated water back into the sink (j). Table 1 below shows the equipment used for each part of the experimental test rig as outlined in Figure 1.

Table 1: Equipment and materials used in construction of experimental set-up.

Equipment/Material:	Description:
(a) tap water [8]	Water from the analytic lab on the HSLU campus Horw.
(b) FP1.400 KPDCB-4 [9]	Diaphragm pump to circulate water.
(c) AS3002F [10]	Valve for fine control of HTF through the heat exchanger.
(d) Typ 8077 [11]	Oval gear flow sensor for small flow rates.
(e) heating elements [12]	Heat source for heat exchanger.
(f) Armaflex insulation [13]	20 mm of insulation around heat exchanger.
(g) copper [14]	Copper for heat exchanger.
(h) PT-100 [15]	4-wire temperature sensors.
(i) JUMO	Power supply and data logger.

The tungsten shell was replaced with copper for its high thermal conductivity and machinability (d) and (e). A layer of PTFE (Teflon) was used to maintain a boundary condition set in the simulated environment (c). It was chosen for its high operating temperature and low thermal conductivity [16–18]. Water was used as the heat transfer fluid (HTF) for its high thermal capacity and working temperature range [8].

A perpendicular cross-fin arrangement of channels consisting of two-layers was designed. Figure 2 below shows an exploded view of the design which was realized for simulation and testing.

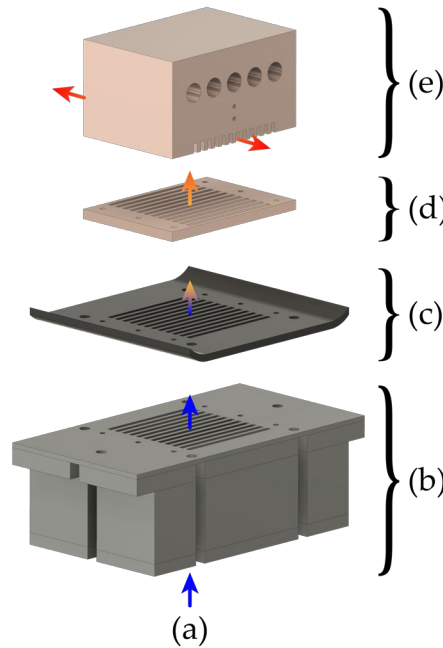


Figure 2: Exploded view of design concept.

Water passed thru an inlet (a) to a reservoir (b) where the flow is split into channels. It then flows past the 3 mm thick PTFE gasket (c), and into the first layer of channels in the copper layer (d). Finally, the water enters the second layer of channels machined into the heated copper block (e) and exits the channels to the front-right and back-left. The copper block (e) dimensions were 50 mm wide by 70 mm long by 40 mm tall. Channel dimensions were 2 mm in width and 4 mm in height with 2 mm thick fins to accommodate machining the copper block, copper plate, and steel plate with an in-house CNC machine. This represents an area ratio of ~ 3.6 with a fin efficiency of ~ 0.57 (Appendix A, Figure 7).

The working principles of the copper block were to apply a heat flow from a solid source to a liquid regime via conduction and convection. Figure 3 below shows the working relationship for the experimental test rig.

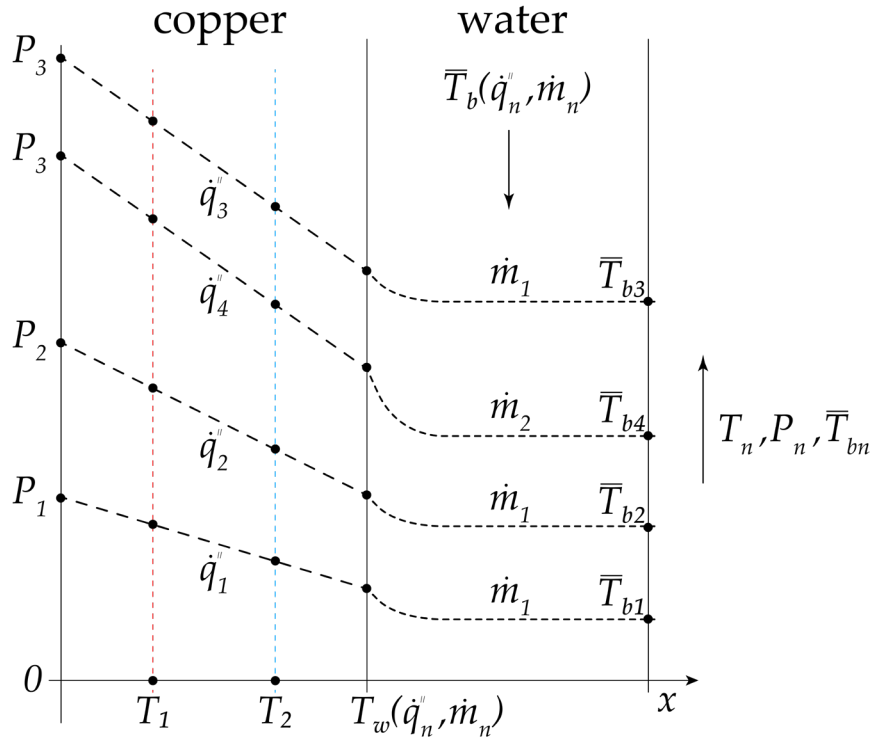


Figure 3: Working principles of the experimental test rig.

Heating power (P_n) applied via heating elements at different levels flow from left to right. The heat passes two temperature sensors (T_1, T_2) at a distance apart (x_1, x_2) and is used to determine specific heat flux (\dot{q}'') via Fourier's Law of heat transfer in one-dimension as shown in equation (1) with the thermal conductivity of copper (λ_{Cu}).

$$\dot{q}'' = \lambda_{Cu} \cdot \frac{\Delta T_{12}}{\Delta x_{12}} \text{ [W/(m}^2 \cdot \text{K)]} \quad (1)$$

Heat flow from the solid copper block to water via a difference between the wall temperature (T_w) and the average bulk water temperature (\bar{T}_{bn}). Increasing heating power ($P_1 \rightarrow P_2 \rightarrow P_3$) while holding fluid flow (\dot{m}_1) constant raises specific heat fluxes ($\dot{q}_1'' \rightarrow \dot{q}_2'' \rightarrow \dot{q}_3''$) at higher overall temperature levels shown in Figure 3. As fluid flow is increased ($\dot{m}_1 \rightarrow \dot{m}_2$) while holding power constant (P_3) maintains the specific heat flux ($\dot{q}_3'' \rightarrow \dot{q}_4''$) at a lower overall temperature level.

2.2 Simulation and experiment

The PEXS simulation was designed with the CAD rendering in Figure 2 above. Two lines of symmetry were used to reduce the computational domain and simulation runtime. Figure 4 below shows the simulated domain as designed.

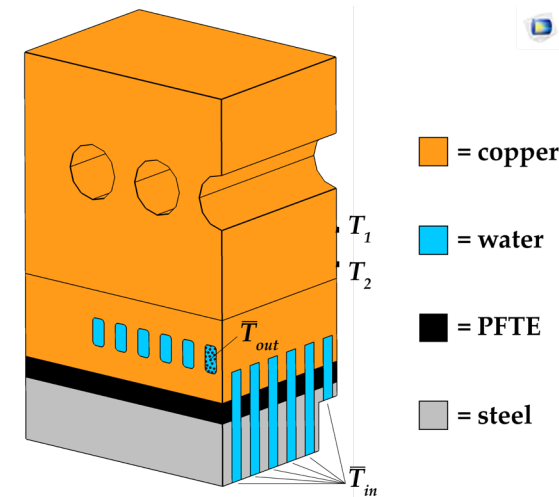


Figure 4: Simulation domain.

Symmetric faces run along the front-right and back-right side leaving external faces on the front-left, back-left, top, and bottom sides of the geometry. External faces were treated as adiabatic. Points T_1 and T_2 were referenced to determine the specific heat flux for the copper block. The simulation used laminar flow in the fluid domain. The mesh consisted of 975'504 elements. Nine flow rates were simulated across 7-9 heating power levels for a total of 75 individual results. Fluid inlet temperatures were set to 15°C while outlet temperatures were determined by averaging the values over the outlet surface.

The PEXS experiment was run to include the same flow rates and heating power levels as a basis for comparison. Figure 5 below shows the assembled experimental test rig.

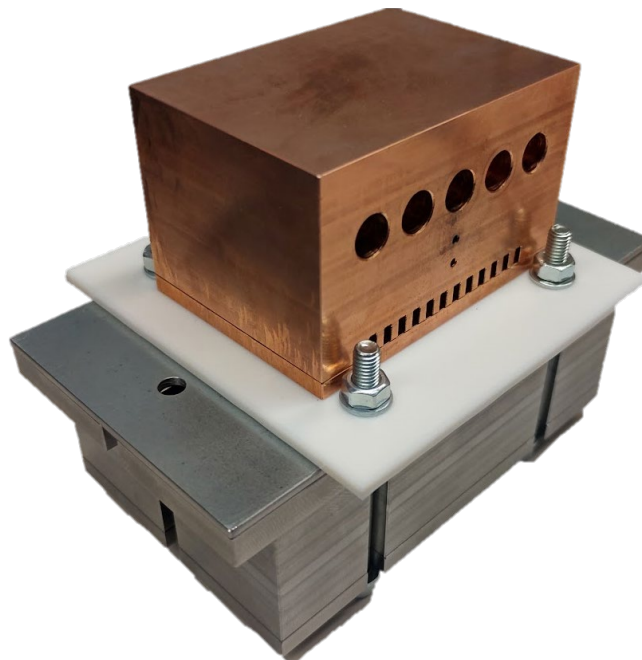


Figure 5: Experimental test rig.

The small holes in the middle of the front-right face were used to insert temperature sensors and determine the specific heat flux while the large holes were used for the heating elements. Outlet temperatures

were measured with an in-situ temperature sensors (PT-100) just outside the two central outlets of the copper block on one side (a) and using a collector for both central channels on the other (b). Figure 6 below shows the temperature sensor at the outlets, inside the copper block, and heating elements.

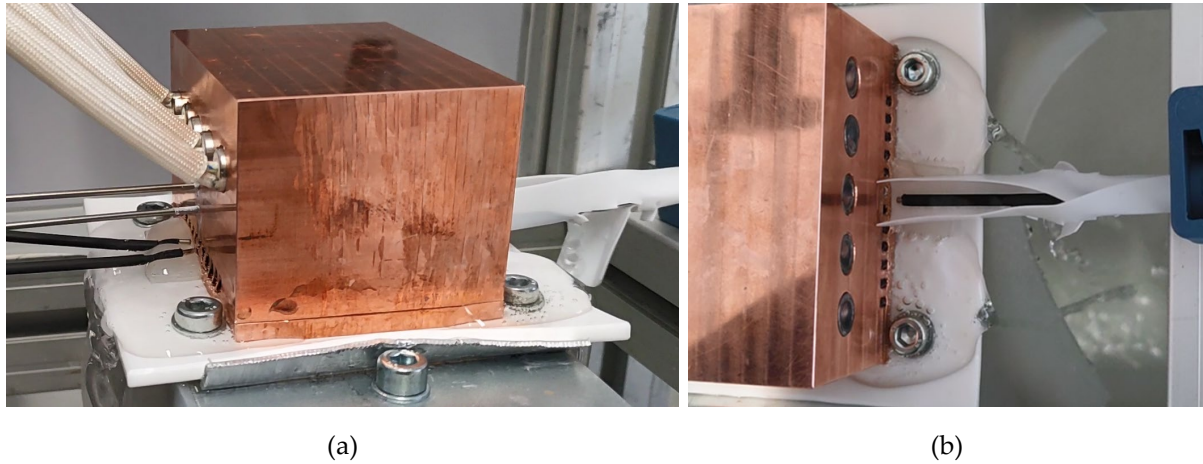


Figure 6: Heat flux temperature sensors and heating elements (a); Outlet temperature sensors (a) and (b).

The outlet temperature sensors for each outlet of the central channel (Figure 6a) and combined outlets of central channels (Figure 6b) were coated in a polymer used for insulating wire. This was to encourage a more accurate measurement of the fluid outlet temperature without the influence of air temperature on the sensors.

The heat flux temperature sensors (Figure 6a) were embedded inside the copper block 25 mm (half the block) from the insertion point. These sensors were coated with a silicone thermal paste to minimize thermal resistance between the copper block and sensors. These sensors were located 5 mm apart and an average of 8.5 mm above the bottom of the second layer of channels.

The final temperature sensor was placed in the tube supplying coolant thru the inlet to the reservoir block (Figure 2b). Figure 7 below shows the placement of the sensor.



Figure 7: Inlet temperature sensor.

Experimental measurements were recorded using the following steps. First, the desired flow rate was set using the diaphragm pump, flow meter, and digital transmitter/controller shown in Figure 8 (a-c) respectively without any external heating.



Figure 8: Diaphragm pump (a); Oval-wheel flow meter (b); Transmitter/controller (c).

A series of heating power levels were applied to the block while temperature was monitored. When temperature levels became stable (neither increasing nor decreasing in the span of 2 min), a measurement point was captured using the average of 100 temperature measurements per second, for a total of 120 seconds. Table 2 below shows the flow rates and power levels tested for comparison with simulations.

flow rate [l/min]	power level [W]
0.60	157.5
0.72	315.0
0.84	472.5
0.96	630.0
1.08	787.5
1.20	945.0
1.32	1102.5
1.44	1260.0
1.56	1417.5

Table 2: Flow rates and power levels evaluated.

Several combinations using low flow rates and high power were not measured to ensure that the boiling point of water was avoided by a safe margin.

2.3 Simulation and experimental comparison

A measurement and calculation scheme were structured to provide a fair comparison of the simulated and experimental set-ups. Both environments were evaluated for average conditions determined at the central point of the simulated and experimental domains. The primary basis to compare the output from simulations and experimental measurements was to estimate the heat transfer coefficient between the solid block of copper and water within the channels. Basic thermodynamic theory was applied to both

simulated and experimental domains to establish a common metric for comparison. The first comparison was to determine the heat flux density. As shown in Figure 9 below, temperatures (T_1, T_2) were determined at the center of the copper block for each of the heating power levels. The difference in temperature (ΔT_{12}) was used to determine the specific heat flux density (\dot{q}_{12}) with equation (1). The specific heat flux density and average temperature between points (\bar{T}_{12}) were assumed to occur at the midpoint between measurement points and the temperature gradient was linear. The temperature gradient along with the average temperature between measurement points were used to extrapolate the average wall temperature along the fluid channel (\bar{T}_w) with equation (2) below as shown in Figure 9.

$$\bar{T}_w = \bar{T}_{12} - \Delta T_{12} \cdot \frac{dw}{2dx} \quad (2)$$

Figure 9: Average wall temperature estimation.

The bulk-average temperature of the fluid (\bar{T}_b) was determined by the average of the average outlet temperature (\bar{T}_{out}) and the average inlet temperature (\bar{T}_{in}) as shown in equation (3).

$$\bar{T}_b = \frac{(\bar{T}_{out} + \bar{T}_{in})}{2} \text{ [K]} \quad (3)$$

The average outlet temperature in the simulation was the average over the central outlet surface whereas \bar{T}_{out} in the experiment was a weighted average over 3 sensors. The combined measurement on one side of the copper block (T_3) measured two channels while the sensors on the other side measured one channel each. Equation (4) shows the weighted average outlet temperature from the experimental measurements.

$$\bar{T}_{out} = \frac{(2 \cdot T_3 + T_4 + T_5)}{4} \text{ [K]} \quad (4)$$

The quantity of heat transferred from copper block to water (\dot{Q}) was determined using a simple energy balance as shown in equation (5) below.

$$\dot{Q} = \dot{m} \cdot C_p(\bar{T}_b) \cdot (\bar{T}_{out} - \bar{T}_{in}) \text{ [W]} \quad (5)$$

The average heat transfer coefficient of the fluid (α) was calculated by dividing \dot{Q} by the area of the central channels (A) and the temperature difference of the average wall temperature (\bar{T}_w) and the average bulk fluid temperature (\bar{T}_b) as shown in equation (6) below.

$$\alpha = \frac{\dot{Q}}{A \cdot (\bar{T}_w - \bar{T}_b)} \text{ [W/(m}^2 \cdot \text{K)]} \quad (6)$$

Table 3 below shows a summary of the quantities evaluated in the simulation and experimental measurements.

quantity	description
$(\bar{T}_{out} - \bar{T}_{in})$	difference between average inlet and average outlet fluid temperatures
\dot{Q}	heat flow into the central channels
\dot{q}''	specific heat flux density
α	fluid heat transfer coefficient

Table 3: Summary of quantities compared.

3 Results and discussion

This section provides the results of both simulated results and experimental measurements in a format for comparison. A short discussion follows each quantity explaining the similarities or differences between values.

3.1 Simulation vs. experimental set-up

The difference between the average inlet and average outlet temperatures of the fluid ($\Delta\bar{T}_f$) were analyzed as a first comparison of the performance of the simulation and experiment. Figure 10 below shows $\Delta\bar{T}_f$ plotted against flow rate and heating power.

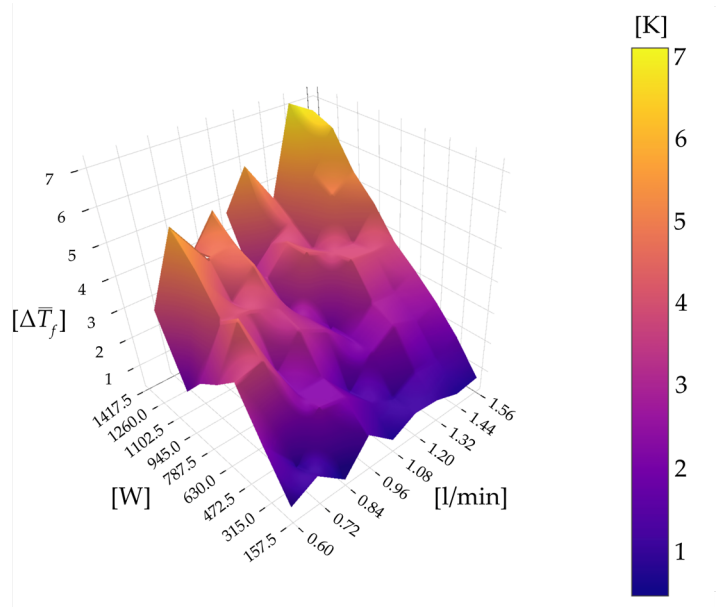


Figure 10: Absolute difference of the average inlet and outlet temperatures between simulation and measurements.

The trend in Figure 10 shows greater deviations for $\Delta\bar{T}_f$ with higher flow and heating rates. Another perspective is given by the relative change in $\Delta\bar{T}_f$ between simulation and experiment as this also factors in the magnitude of $\Delta\bar{T}_f$. Figure 11 below show the relative difference between simulation and experiment of \bar{T}_{in} and \bar{T}_{out} .

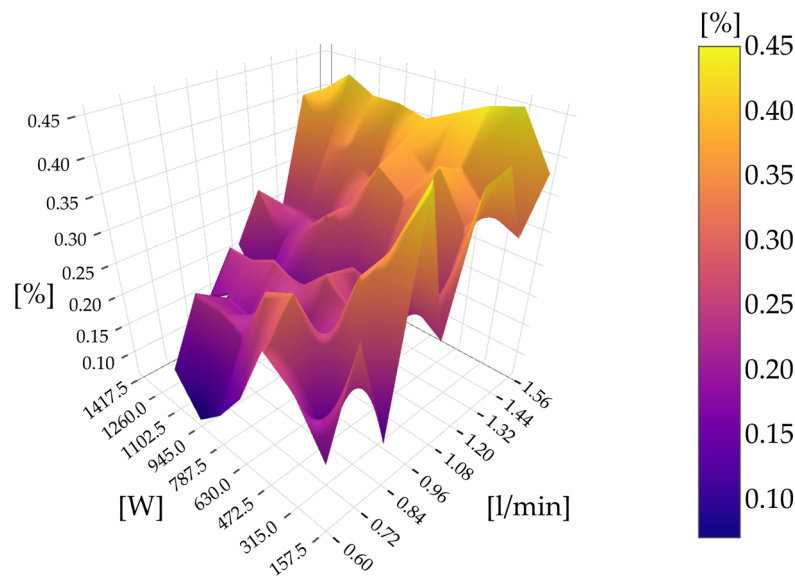


Figure 11: Relative difference between simulation and experiment for average inlet and outlet temperatures.

The data from this perspective supports the trend of higher deviations in $\Delta\bar{T}_f$ in Figure 10 with additional trend of decreasing proportional deviations with increasing heating power. This shows relative deviations in $\Delta\bar{T}_f$ between simulations and experiments increase slower than the absolute deviations in $\Delta\bar{T}_f$.

Heat flow into the analyzed channels (\dot{Q}) was a key quantity for determining the specific heat flux density (\dot{q}'') and fluid heat transfer coefficient (α). Table 4 below shows the calculated heat flow into the central channels using equations (4) and (5).

\dot{V} [l/min]	1.56		1.44		1.32		1.20		1.08		0.96		0.84		0.72		0.60	
Power [W]	sim [W]	exp [W]	sim [W]	exp [W]	sim [W]	exp [W]	sim [W]	exp [W]	sim [W]	exp [W]	sim [W]	exp [W]	sim [W]	exp [W]	sim [W]	exp [W]	sim [W]	exp [W]
1417.5	301	180	298	179	295	225	292	211	288	230	—	—	—	—	—	—	—	—
1260.0	269	153	267	178	264	201	261	209	258	221	255	195	252	209	—	—	—	—
1102.5	237	140	235	153	233	179	230	172	227	186	225	172	222	176	218	169	214	186
945.0	205	120	203	141	201	143	199	141	197	165	195	144	192	156	189	146	184	172
787.5	172	104	171	107	169	109	167	139	166	130	164	124	162	123	158	125	155	137
630.0	139	81	138	90	137	92	136	106	134	98	133	96	131	107	128	90	125	104
472.5	106	60	105	66	104	64	103	73	102	87	101	76	99	78	97	66	94	69
315.0	72	40	71	47	71	48	70	56	69	51	68	44	67	44	65	58	64	49
157.5	37	22	36	25	36	21	36	21	35	27	35	19	34	30	33	23	32	27

Table 4: Calculated heat flows into analyzed channels for simulations and experiments.

A comparison of each case resulted in lower amount of heat entering the channels experimentally versus simulation with an average difference of 27%. Specific heat flux density was calculated with equation (1). Table 5 below shows the comparison of specific heat flux densities for each case as the deviation of the simulation from experiment in %.

\dot{V} [l/min]	1.56	1.44	1.32	1.20	1.08	0.96	0.84	0.72	0.60
Power [W]	sim vs. exp	sim vs. exp	sim vs. exp	sim vs. exp	sim vs. exp	sim vs. exp	sim vs. exp	sim vs. exp	sim vs. exp
1417.5	-11.9%	-10.8%	-8.6%	-8.5%	-4.6%	—	—	—	—
1260.0	-14.4%	-13.4%	-9.9%	-8.0%	-6.0%	-15.7%	-12.3%	—	—
1102.5	-14.9%	-12.3%	-12.4%	-8.4%	-7.1%	-18.0%	-15.6%	-11.6%	-11.0%
945.0	-15.9%	-13.3%	-11.2%	-8.6%	-6.2%	-14.2%	-14.8%	-12.3%	-10.8%
787.5	-17.0%	-14.9%	-11.4%	-8.5%	-6.7%	-12.8%	-16.4%	-12.3%	-12.3%
630.0	-18.5%	-15.5%	-12.9%	-9.7%	-10.0%	-14.3%	-13.7%	-15.3%	-16.5%
472.5	-20.2%	-16.8%	-12.9%	-10.8%	-7.5%	-20.1%	-18.8%	-13.8%	-14.4%
315.0	-24.2%	-20.0%	-19.5%	-17.0%	-10.5%	-24.0%	-19.5%	-15.6%	-16.1%
157.5	-33.9%	-28.2%	-25.9%	-21.9%	-20.8%	-29.6%	-28.9%	-31.9%	-30.5%

Table 5: Specific heat flux densities for simulations and experiments.

In all cases the heat flux density was lower in the simulation than in the experiment. However, it is possible this was a result of measurement error during the experiments. The simulation did not have any disruption nor discontinuity in the calculation of the specific heat flux density. This was not the case for the experimental tests. Holes were drilled into the copper block to insert probes to measure temperature. These holes were placed one over the top of another and may have created a “thermal shadow” whereby the added thermal disturbances depressed the temperature recorded at T_2 . In addition, the experimental test block was subject to cooling to the ambient which may have caused additional cooling at measurement point T_2 . Both these combined factors increase the temperature gradient calculated in equation (1) and thus inflating the specific heat flux density in the experiments relative to the simulations.

The last quantity compared was the fluid heat transfer coefficient (α). Using equations (2-6) and the fluid heat transfer coefficients for simulations and experiments were calculated. Figure 12 below shows the calculated values for each flow rate and heating power simulated with an “x” and for measurements with a “—”. Averages for all power levels at a constant flow rate are shown as green dots in the simulation and red diamonds for experimental measurements.

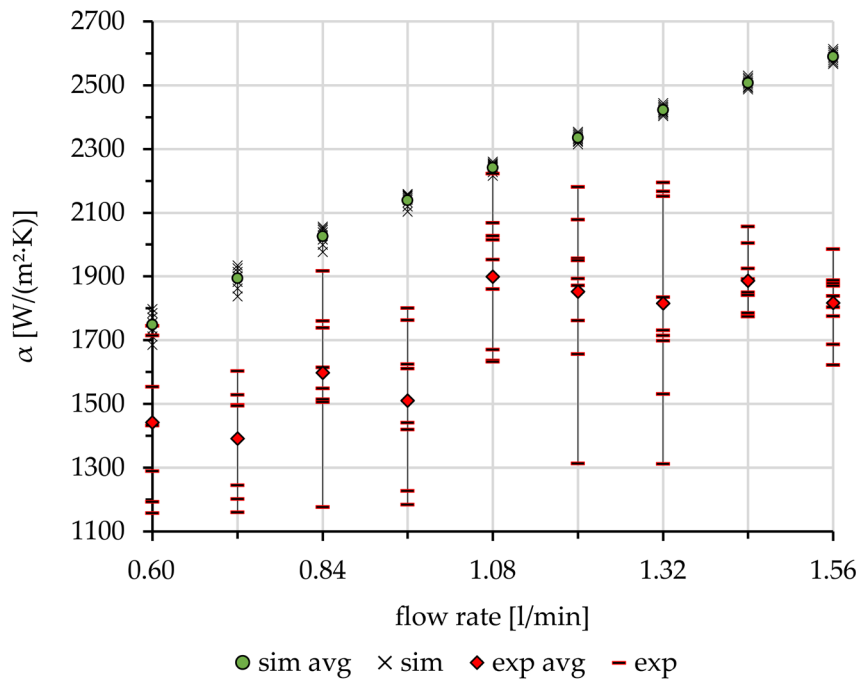


Figure 12: Fluid heat transfer coefficients.

The experimental results were up to 45.4% lower than simulated with an average of 23.4% for all measurements. Table 6 below shows the full results of both simulated and experimental results for the fluid heat transfer coefficient (α) in $W/(m^2 \cdot K)$.

\dot{V} [l/min]	1.56		1.44		1.32		1.20		1.08		0.96		0.84		0.72		0.60	
Power [W]	sim	exp	sim	exp	sim	exp	sim	exp	sim	exp	sim	exp	sim	exp	sim	exp	sim	exp
1417.5	2614	1987	2530	1851	2444	2195	2354	1958	2260	2016	—	—	—	—	—	—	—	—
1260.0	2608	1839	2524	2006	2438	2167	2349	2181	2256	2224	2159	1802	2056	1918	—	—	—	—
1102.5	2602	1878	2518	1892	2433	2152	2343	1951	2251	2028	2155	1764	2051	1761	1935	1605	1798	1716
945.0	2596	1871	2513	2058	2427	1836	2339	1762	2247	2069	2151	1626	2046	1740	1926	1530	1785	1746
787.5	2590	1890	2507	1787	2422	1699	2334	2079	2243	1861	2146	1612	2039	1550	1914	1498	1771	1555
630.0	2584	1805	2502	1842	2417	1733	2331	1895	2239	1672	2141	1442	2029	1616	1900	1246	1754	1433
472.5	2578	1687	2496	1776	2413	1533	2327	1657	2235	1953	2132	1420	2015	1507	1883	1161	1735	1159
315.0	2572	1623	2492	1842	2409	1716	2322	1873	2228	1637	2120	1185	1999	1177	1862	1496	1712	1194
157.5	2567	1776	2487	1926	2404	1313	2315	1314	2216	1633	2103	1229	1977	1515	1838	1202	1685	1290

Table 6: Fluid heat transfer coefficient result for each compared case.

Several assumptions and observations were responsible for the differences in simulated results and experimental measurements. The construction of experimental set-up had an added thermal resistance between the first- and second-layer channels which the simulation did not. This presented itself as a very thin air gap which would have inhibited heat flow from second-layer fins (Figure 2 (d)) to the first-layer fins (Figure 2 (e)). As a result, the calculated heat transfer from the first- to second-layer fins was lower in experiments than simulations.

A complex geometry used for this experiment made it nearly impossible to measure the wall temperatures. The assumption to estimate a wall temperature using the temperature gradient from within the copper block was applied. At best, this estimated the wall temperature at the bottom of the second-layer channels with overestimated values progressing upstream into the second-layer fins. The wall temperature errors were compounded in the experimental set-up with the additional thermal resistance thus depressing the actual values lower than in the simulations. In addition, the calculated temperature gradient had its own measurement errors with an artificial decrease in T_2 .

Finally, the use of tap water was problematic for the temperature range applied to the constructed experiment. The internal structure of the experiment had layers that had small but significant edges or grooves which harbored air bubbles upon wetting the heat exchange surfaces. Uneven surfaces make it possible for small bubbles to fix themselves or form with sufficient shear stress around small geometries. This was directly observed during measurements. Figure 13 below shows a bubble formed on the end of the inlet temperature sensor heating of the fluid had occurred.



Figure 13: Bubble on inlet temperature sensor.

In addition, tap water has dissolved gasses (mainly air) which become less soluble with increasing temperature and form bubbles in the fluid. Small bubbles appeared at the outlets and on visible surfaces with sharp corners or edges. Figure 14 below shows heavy outgassing of dissolved air from heating tap water in the heat exchanger.

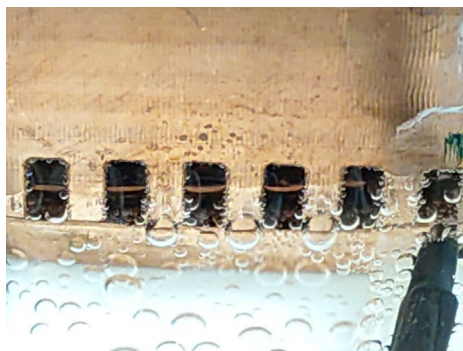


Figure 14: Outgassing of air from tap water.

The formation of bubbles on internal surfaces reduced the wetted surface area of the heat exchanger, created stochastic flow patterns, and inhibited heat flow from the walls to the fluid. This is further supported by the calculated values of α for the experiments being lower than simulations.

4 Conclusion and future development

4.1 Conclusion

In conclusion, it is reasonable to deduce the simulated results broadly estimated the performance of experimental measurements. A recommendation for further development of the model to include some features important to heat transfer is necessary to bring simulated results in better agreement with experimental measurements. The inclusion of a thermal resistance between fin layers and the inclusion of an insulated layer along with ambient conditions would be an improvement. A reduction in error would better support the use of this simulation tool for the dimensioning and design of a PEX for cooling a fusion reactor core. Complementary to simulation improvements, experimental improvements would help to reduce further features observed during experimentation. Expanding the geometric domain would increase the volume to surface area ratio which would reduce effects on the domain from thermal interactions on peripheral surfaces exposed to the ambient. Furthermore, the interfering effects of probes embedded in regions where heat flow is critical would be reduced and thus more accurate measurements. A thicker layer of insulation could be incorporated with a new geometry further mitigating losses to the environment. Improved versions of experimental set-ups using water should consider the formation of bubbles in small geometries. Surface treatments to increase surface smoothness and eliminate seams and boundaries would be recommended. The emergence of air bubbles from outgassing could be addressed by preheating the fluid to expel dissolved gasses before experimentation. Otherwise, it is concluded that an alternate heat transfer fluid be used which has a lower content of dissolved gasses and/or has a higher solubility for gasses thus less problems with the formation of bubbles when heated.

4.2 Future development

Designing, manufacturing, and testing a heat exchanger to safely operate a fusion reactor is an ongoing field of research. The study in this report employed a geometry of multi-layered channel flow which enhanced swirling and replacement of cooler fluid to hot surfaces. Future experimental set-ups should aim to incorporate the proposed materials (e.g., FLiBe, tungsten, and Inconel) at temperatures representative of proposed working conditions as outline in Appendix A. Recommendations from CFS included the following remarks for system modeling, evaluation, and experimentation:

- An expansion of the average temperature difference between inlet and outlet to 140 K.
- Average values for the heat flux density emerging from the vacuum vessel.
- A move to incorporate turbulent flows and simulations.
- Limit or eliminate splitting flow patterns to reduce pressure drop in the channels.
- The substitution of copper-tungsten alloys for pure tungsten to increase thermal conductivity of non-structural geometric features (i.e., fins) which would braze well with vanadium.

Appendix A

Article

Blanket Cooling of a Fusion Reactor

Robert Beaufait ^{1*}, Ludger Fischer ²

^{1*} Competence Center Thermal Energy Storage (CCTES), Lucerne University of Applied Sciences and Arts, Technikumstrasse 21, 6048 Horw, Switzerland; robertpeter.beaufait@hslu.ch (R.B)

² Competence Center Thermal Energy Storage (CCTES), Lucerne University of Applied Sciences and Arts, Technikumstrasse 21, 6048 Horw, Switzerland; ludger.fischer@hslu.ch (L.F.)

Abstract: Nuclear fusion is the gateway to a whole new paradigm of energy and a strong candidate to decarbonize electricity generation on a global scale. With recent developments in high temperature super-conducting magnets, the race is on to develop sub-systems which will support a commercially viable fusion reactor for use as a thermal power plant. Fusion of lighter elements create enormous heat which must be transferred away from the reactor core. These intense conditions require novel approaches in efficiently transferring very high heat loads into useable thermal energy without compromising structural integrity of the reactor core and surrounding components. This report outlines the concept for a fundamental approach to solve the heat transfer problem as proposed by Commonwealth Fusion System's design for a fusion reactor. A literature review was conducted for other applications that could serve as inspiration as well as material properties and machining methods for the proposed power exhaust system. A dive into theoretical thermodynamic and fluid dynamic characteristics of plate heat exchangers and finned surfaces was conducted for a fundamental perspective. A laminar flow regime was studied for the purpose of setting the floor for energy needed to pump coolant while simultaneously representing the least favorable heat transfer regime between a solid surface and a fluid. The results served as a basis for dimensioning and executing numerical simulations as a means for a first look into a solution of this heat transfer problem. Results are compared with the theoretical conclusions and judged based on constraints of the system. Recommendations are made for continued development of a corresponding system.

Citation: To be added by editorial staff during production.

Academic Editor: Firstname Last-name

Received: date

Revised: date

Accepted: date

Published: date



Copyright: © 2023 by the authors. Submitted for possible open access publication under the terms and conditions of the Creative Commons Attribution (CC BY) license (<https://creativecommons.org/licenses/by/4.0/>).

Keywords: vacuum vessel cooling; high-power heat transfer; blanket cooling; fusion energy

1. Introduction

Energy from nuclear fusion of two lighter elements represents the next paradigm in energy generation. It represents the most common type of observable reaction in the universe, the enormous energy released by stars, and the incredible potential it could provide to humanity [1–3]. These intense reactions create extremely high specific heat fluxes. The Competency Center Thermal Energy Storage (CCTES) is conducting a research study based on principle ideas created by Commonwealth Fusion Systems (CFS) to develop a concept for a part of the power exhaust system (PEXS) necessary for the removal of heat from a fusion reactor core. In a former CFS publication, the basic engineering principles for the blanket

cooling system within the affordable compact robust (ARC) reactor were described. However, a design proposal for the heat exchange surfaces and heat transfer fluid has not been published yet. [4]. The reactor core consists of the fusion fuels reacting in a magnetically confined vacuum vessel requiring cooling. Vacuum vessel heat flux density reaches a peak of 12 MW/m² which needs to be removed via FLiBe (Fluoride-Lithium-Beryllium) molten (liquid) salt to maintain material integrity. The intention of this work is to suggest and examine one potential solution approach: A novel design proposal for removing high end vacuum vessel heat fluxes using a FLiBe molten salt heat transfer fluid. The design proposal is based on data from CFS and former research work at CCTES. The design proposal includes incorporation of manufacturing possibilities and general design to keep the inner (thin) shell mechanically stable, to allow for high heat transfer coefficients by forced convection (or even free convection) and for mass transfer exchange with the molten salt reservoir (for transport of the heat to the bulk FLiBe tank). A general layout of the design is developed, general assumptions of required flow rates of FLiBe and a possible way to evenly distribute this all over the 300 m² of blanket surface is shown, the blanket surface will be structured with a grid consisting of fins, and a detailed numerical calculation of the local heat transfer under such conditions is executed. Starting with a parameter study of the influence channel dimensions and fin width, the general feasibility in terms of heat transfer and pressure drop for FLiBe and laminar flow shall be examined.

2. Materials, Theory, and Methods

2.1. Materials

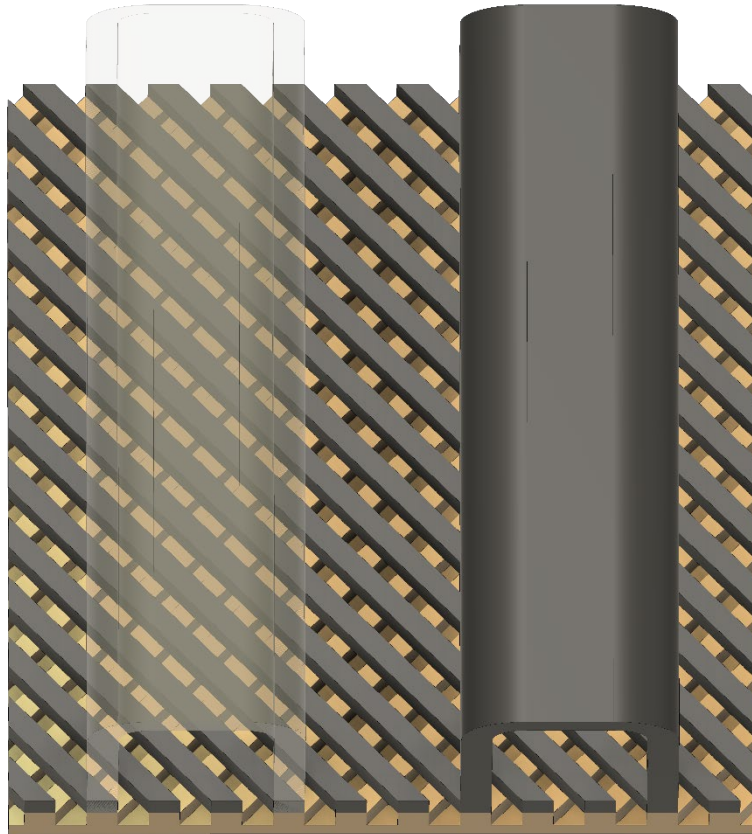
Three main materials are needed to construct the heat exchanger or PEXS. Tungsten (W, Wolfram) is the proposed material for the plasma facing surface responsible for transferring heat to the molten FLiBe salt in the ARC reactor design. It has a high melting temperature of 3400 °C, low vapor pressure, and high tensile strength [5,6]. Tungsten is the material of choice in several divertor designs including ITER (International Thermonuclear Experimental Reactor) for its high thermal conductivity ($k_W \sim 175$ W/(m·K)), high temperature operating range (~ 1500 K), and resistance to plasma erosion [4,7,8]. It is proposed to use a plasma facing layer as thin as possible to minimize thermal resistance while maintaining structural integrity during the operating life cycle.

Above the Tungsten layer is the fluid responsible for capturing and removing heat from the plasma facing surface. The fluid proposed by the CFS paper [4] is the use of FLiBe (LiF – BeF₂; 66 mol%, 34 mol%). FLiBe has several engineering advantages for use as a coolant in a magnetically confined plasma fusion reactor. It exhibits a favorable operating temperature range between 800–875 K, performs well as a radiation shield, and has favorable flow characteristics [9–11]. For the proposed FLiBe operating temperature (800 ~ 875 K) the dynamic viscosity of FLiBe is approximately 10 times higher than water at room temperature (293 K). Table 1 outlines the recommended values for FLiBe over a liquid temperature range between melting (732 K) and boiling (1703 K) points [12].

Table 7. Material properties of FLiBe [12].

Parameter	Correlation	Units	Uncertainty
density	$\rho = 2413 - 0.488 \cdot T[\text{K}]$	kg/m ³	2%
heat capacity	$C_p = 2386$	J/(kg·K)	3%
dynamic viscosity	$\mu = 0.116 \cdot e^{(3755/T[\text{K}])}$	mPa·s	20%
thermal conductivity	$k = 1.1$	W/(m·K)	10%

The design proposed in this paper is a super-structure of Inconel 718 tasked with distributing FLiBe to the tungsten layer and providing structural support to the “cool” side of the PEXS. It operates at a lower temperature than plasma facing surfaces and provides a structural level of support to the inner tungsten layer. Inconel was chosen for its high melting temperature ($\sim 1480 - 1610$ K), very high yield and tensile strength, and excellent weldability with itself and tungsten [13–15]. Figure 1 below illustrates the conceptual design of the channeled tungsten plasma facing surface (orange in the back) attached to a second set of Inconel 718 channels (dark gray). FLiBe capillary channels are shown over the top of the entire construction.

**Figure 15:** General design concept with distribution channels (the left one semi-transparent for better insight into the lower grid).

2.2. Theory

A full understanding of heat transfer and the effects of material extended away from a surface is requisite to properly evaluate designs which best conform to the boundary conditions. Table 2 below shows the boundary conditions of the PEXS which must not be exceeded. This set of boundary conditions are considered nominal operating conditions as outlined by CFS.

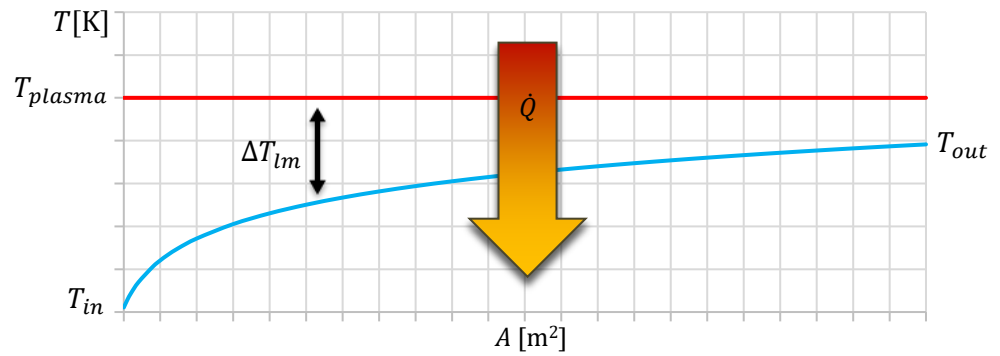
Table 8. Boundary conditions of vacuum vessel cooler [4].

Boundary Condition	Value	Quantity
max heat flux density	$\sim 12 \text{ MW/m}^2$	\dot{Q}/A
T_{\max} tungsten	1500 K	T_{plasma}
ΔT_{\max} FLiBe	$\sim 75 \text{ K}$	$(T_{\text{out}} - T_{\text{in}})$

2.2.1 Heat Transfer

Heat from the inner core to the tungsten shell is transferred mainly by radiation. The following theory assumes the maximum tungsten temperature will be maintained by an equilibrium of radiation from the core to tungsten and convective heat transfer from tungsten to FLiBe. The boundary conditions were conceptualized in terms of heat transfer using the general theory for plate heat exchangers. Figure 2 below qualitatively shows the evolution of FLiBe temperature as it passes through the tungsten structure. It is governed by the following equation.

$$\dot{Q} = \dot{m} \cdot C_p \cdot (T_{\text{out}} - T_{\text{in}}) = h \cdot A \cdot \Delta T_{lm} \quad (1)$$

**Figure 16:** Generalized heat exchanger temperature profile.

\dot{Q} is the heat flux in watts, \dot{m} the FLiBe mass flow in kg/s, C_p the specific heat capacity J/(kg·K), h the overall heat transfer coefficient W/(m²·K), and A the area of the plasma facing surface. ΔT_{lm} is the logarithmic mean temperature difference (LMTD) between the heat source and heat sink. It is defined in the equation (2) below and accounts for a non-uniform temperature difference along the path of the fluid. T_{plasma} is the temperature of the tungsten shell on the inner plasma facing side.

$$\Delta T_{lm} = \frac{(T_{\text{plasma}} - T_{\text{in}}) - (T_{\text{plasma}} - T_{\text{out}})}{\ln \frac{(T_{\text{plasma}} - T_{\text{in}})}{(T_{\text{plasma}} - T_{\text{out}})}} \text{ [K]} \quad (2)$$

Equation (1) can be rearranged to give us the minimum required heat transfer coefficient (h_{\min}), and minimum area specific FLiBe mass flow (\dot{m}_{\min}/A) as show in equations (3) and (4) respectively.

$$h_{\min} = \frac{\dot{Q}}{A} \cdot \frac{1}{\Delta T_{lm}} \text{ [W/(m}^2 \cdot \text{K)]} \quad (3)$$

$$\frac{\dot{m}_{\min}}{A} = \frac{\dot{Q}}{A} \cdot \frac{1}{C_p \cdot (T_{\text{out}} - T_{\text{in}})} \text{ [kg/(m}^2 \cdot \text{s)]} \quad (4)$$

Using equations (2) – (4), and the boundary conditions in Table 2, a $\Delta T_{lm} \sim 660 \text{ K}$, $h_{\min} \sim 18 \text{ kW/(m}^2 \cdot \text{K)}$, and a \dot{m}_{\min}/A of $\sim 68 \text{ kg/(m}^2 \cdot \text{s)}$ were

found. These calculated quantities represent the heat flow characteristics to remain within the boundary conditions set forth by ARC reactor design. Figure 3 below shows the proposed ARC reactor operating point in terms of fluid temperature change, LMTD, and h_{min} . This helps to maximize the thermal driving force, keep plasma facing surfaces cooler than the maximum temperatures allowed, and minimize asymmetric thermal stresses across the tungsten elements.

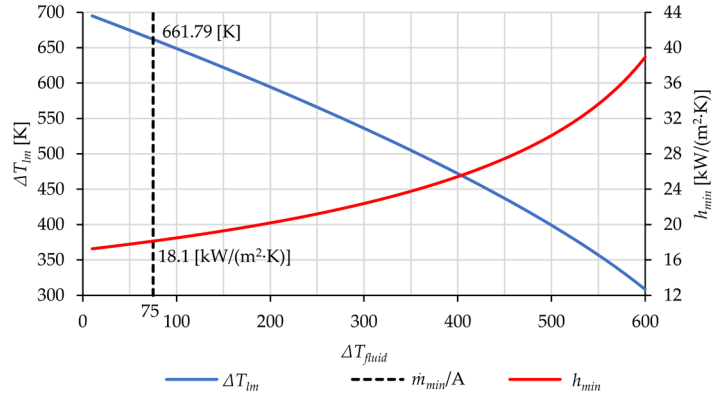


Figure 17: Dependence of LMTD and h_{min} with ΔT_{fluid} and \dot{m}_{min}/A .

The minimum required overall heat transfer coefficient (h_{min}) is a function of tungsten thickness (δ_w) and the minimum average heat transfer coefficient for the fluid surface (α_{min}). Equation (5) below defines α_{min} in terms of these new quantities and is plotted against tungsten layer thickness in Figure 4.

$$\frac{1}{\alpha_{min}} = \frac{1}{h_{min}} + \frac{\delta_w}{k_w} \left[\frac{(m^2 \cdot K)}{W} \right] \quad (5)$$

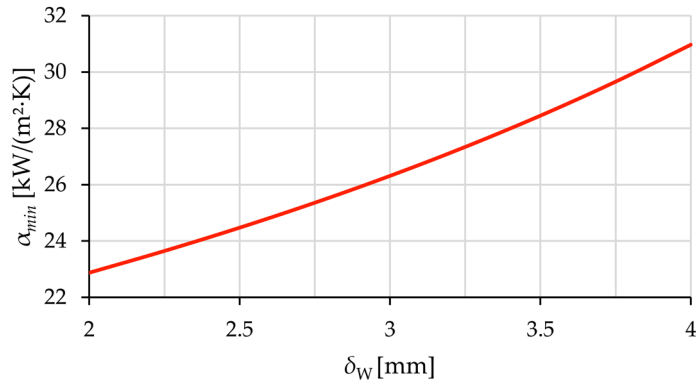


Figure 18: Dependence of α_{min} on the thickness of the inner layer of tungsten and equation (5).

2.2.2. Area Ratio

Geometric features added to a surface increase the surface area and direct fluid flow in an advantageous manner. These geometric features take the form of extended elements, “fins”, which extend away from the plate. The additional area is an advantage as the required α_{min} decreases as the total area of the finned surface (A_{fin}) increases relative to the flat plate area (A_{plasma}). The area ratio (A_r) is defined as A_{fin}/A_{plasma} and can be used to adjust the required α_{min} as a guide for design. Figure 5 below

shows the general concept of increasing the area of a surface with a rectangular fin relative to a non-finned surface.

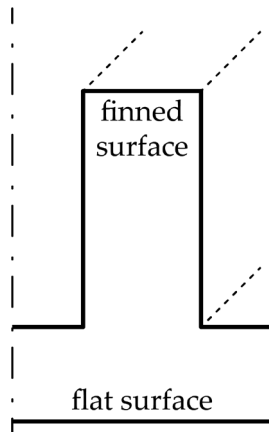


Figure 19: Increased surface area relative to a flat surface by use of fins.

Figure 6 below shows the change in α_{min} with increasing area ratio (A_r). Theoretical thermal performance was analyzed to calculate the effects of different thicknesses of tungsten for the vacuum vessel. It was found that by reducing the thickness of the tungsten to 2 mm and increasing the area ratio significantly reduced α_{min} . Figure 6 below shows the effect of reducing the thickness of the tungsten layer and increasing the area ratio using equation (5).

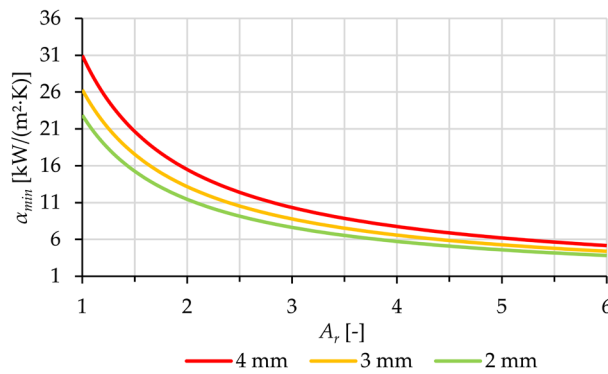


Figure 20: α_{min} as a function of area ratio A_r and tungsten shell thickness.

The higher the area ratio the better chance a design has at successfully meeting the task of transferring the required amount of heat. However, there are limiting factors which constrain the geometry of the fluid surface to a range which is achievable. Assessment of the proposed design used a tungsten plate of 2 mm in thickness and an area ratio > 2 . This represents the minimum vacuum vessel wall thickness and a minimum in thermal resistance to test the thermal performance of the design concept. A thermodynamic design point of an $\alpha_{min} \sim 12000$ [W/(m².K)] is considered in the scope of this study as it is typical of forced convection for non-metallic, single-phase liquids [16].

2.2.3. Fin and Surface Efficiency

The use of fins on a surface constitutes the use of more material above the plate itself. The added material incurs a thermal resistance to heat flow

and thus factors in when determining optimal fin geometry. The use of very long fins is not required to reach the optimal heat transfer rate [17]. Fin efficiency (η_{fin}) is a term which describes the ability to transfer heat of a flat surface or a tube with fins relative to the same surface without fins. It is the ratio of the average temperature difference between the end of geometry extending away from the base and the fluid to the average temperature difference between the base of the surface and the fluid [16]. Equation (6) below summarizes this definition.

$$\eta_{fin} = \frac{\bar{T}_{fin} - \bar{T}_{fluid}}{\bar{T}_{base} - \bar{T}_{fluid}}; 0 \leq \eta_{fin} \leq 1 \quad (6)$$

The efficiency of the fins can be further expanded into an overall surface efficiency η_o . The overall performance of a finned plate is a function of the fin efficiency (η_{fin}), the number of fins (N), the area of each fin (A_f), the total area of the finned plate (A_t), and η_{fin} . Equation (7) below is the overall efficiency of a finned plate flat plate.

$$\eta_o = 1 - \frac{NA_f}{A_t}(1 - \eta_{fin}) \quad (7)$$

The surface efficiency of rectangular fins is plotted below in Figure 7 for an area of 1 m² against A_r , fin thickness (th) fin length (L), and a channel width of 1 mm.

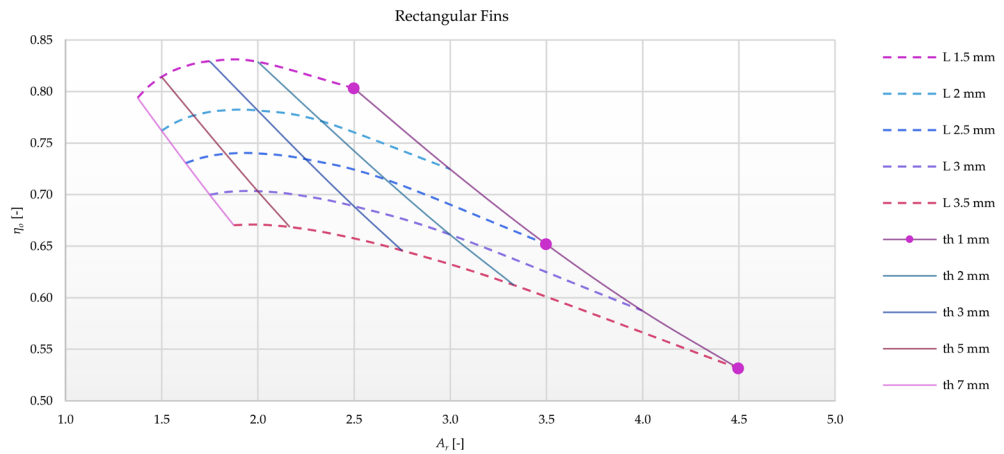


Figure 21: Surface efficiency of rectangular fins on a flat plate.

The primary purpose of optimizing fin geometry is to maximize thermal performance using the least amount of material while the secondary purpose is to promote mixing of cool fluid down to the surface of the finned structure. Rectangular fins were chosen as the best solution as their shape allows for optimal addition of surface area with vertical walls. The five other finned surfaces considered (rectangular pins, triangular/parabolic fins and pins) exhibit poorer overall fin efficiencies at the same area ratios.

The fluid surface geometry is of critical importance to design a structure capable of handling the proposed high heat flux density of the ARC divertor leg. An increased area ratio was achieved by extending material away from the plate surface in the form of rectangular fins as shown in figures 5 and 7. A logical starting point for analysis was using a narrow fin thickness (1 mm), narrow fluid channels (1 mm), and tall fins. Table 3 below shows the dimensions and their corresponding overall fin efficiencies and area ratios.

Table 9. Analyzed fluid surface geometries.

fin length [mm]	η_o [-]	A_r [-]
1.5	~ 0.80	~ 2.5
2.5	~ 0.65	~ 3.5
3.5	~ 0.53	~ 4.5

2.2.4. Pumping power

About 300 m² is needed to envelop the ARC vacuum vessel [4]. Using the calculated area specific mass flow rate (\dot{m}_{min}/A), ~ 20400 kg/s is required to provide the required amount of FLiBe to cool the vacuum vessel shell under the proposed conditions. Minimization of energy use by auxiliary systems to circulate coolant is a priority. The pumping power required has the potential to demand a significant proportion of generated electricity and must be kept to a minimum. Equation (8) below shows the hydrodynamic relationship between pressure loss, fluid mass flow, and electrical power needed to move a fluid with a pump efficiency.

$$P_{el} = \frac{\dot{m} \cdot \Delta p_{loss}}{\rho \cdot \eta_{pump}} \quad (8)$$

Table 4 below displays the estimated pumping power required for the entire proposed PEXS for pressure losses between 1 and 16 bar a pump efficiency (η_{pump}) of 0.85 and an overall coolant mass flow rate of 20400 kg/s for a ~ 200 MW_{el} ARC fusion reactor [18].

Table 10. Estimated electrical power consumption for pumping FLiBe with increasing PEXS pressure losses.

Δp_{loss} [bar]	P_{el} [MW]	% of output
1	1.8	0.9
2	3.6	1.8
4	7.1	3.6
8	14.2	7.1
16	28.4	14.2

2.3. Methods

The boundary conditions relevant for this study are the heat densities to be transferred to the FLiBe heat transfer fluid. The design must be built to minimize fluid pressure losses and thus minimize energy consumption for cooling. Furthermore, uniform temperature gradients within the PEXS material are crucial to maintaining symmetric thermal stresses and material longevity.

A literature review was performed to find any high-power heat transfer applications either in commercial use or lab tested. The results of the literature review served as a basis of inspiration for the initial designs tested in a numerical setting using COMSOL 6.0 [19]. Laminar flow conditions were analyzed as they represent flow conditions which exhibit the lowest pressure losses and worst (in terms of low) heat transfer conditions. This provides a safe-sided starting point in evaluating the feasibility of certain designs with regarding the boundary conditions.

3. Results and Discussion

The results are presented in the following manner: state-of-the-art, design concept, and simulated output. Each section provides the design

development chronologically and therefore, the result of each section is built upon the previous result and presented as such. A short discussion of each step is included with the results.

3.1. State-of-the-art

A literature review was conducted to discover commercial and/or research applications which could serve as a starting point for a design concept. Microchips and integrated circuits have evolved to reach 2.25 MW/m² employing one of the four types of heat transfer: radiation and free convection, forced air-cooling, forced liquid-cooling, and liquid evaporation [20]. Another study examined the thermal exhaust requirements for VLSI (very-large-scale-integrated) circuits [21]. Using a micro-channel structure, laminar flow regime, and employing water as the heat transfer fluid, a heat flux of up to 7.9 MW/m² was achieved with a maximum temperature change of 71 K between substrate and inlet fluid temperature [21]. In this paper it is further suggested a heat flux density of 10 MW/m² is possible by scaling liquid-cooled heat exchanger design to microscopic dimensions. Table 5 below shows the experimental results for several dimensions, fluid pressures (p), flow rates (\dot{V}), and heat flux densities (q). Note specific mass flow rates for water as a coolant, (\dot{m}_w), have been calculated from available data and are of the same order of magnitude as the specific mass flow rates calculated using FLiBe.

Table 11: Experimental VLSI heat sink with water filled microchannels [21].

Exp.	w_c [μm] ¹	w_w [μm] ²	z [μm] ³	p [bar]	\dot{V} [$\frac{\text{cm}^3}{\text{s}}$]	\dot{m}_w [$\frac{\text{kg}}{\text{m}^2\text{s}}$]	$R_{th,max}$ [$\frac{\text{K}}{\text{W}}$] ⁴	q [$\frac{\text{MW}}{\text{m}^2}$]
1	56	44	320	1.034	4.7	47	0.110	1.81
2	55	45	287	1.172	6.5	65	0.113	2.77
3	50	50	302	2.137	8.6	86	0.090	7.90

¹ channel width; ² wall width; ³ channel depth; ⁴ maximum thermal resistance.

A review of heat sinks related to nuclear fission reactors was investigated for a possible corollary for a solution to this heat transfer problem [22]. Nuclear reactors designed to generate electricity exhibit high rates of heat transfer from fuel rods to coolant fluid. Various coolants are used depending on reactor design. An overview in Table 6 below is given to outline potentially suitable solutions.

Table 12: Experimental VLSI heat sink with water filled microchannels [22].

Reactor Type ¹	PWR ^a			BWR/6 ^b	HTGR ^c	LMFBR ^d	GCFR ^e	CANDU PHW ^f
Manufacturer ²	W ^a	B&W ^b	GE ^c	-	-	-	-	-
Coolant	H ₂ O	H ₂ O	H ₂ O	H ₂ O	He	Na	He	D ₂ O
Avg. heat flux ³	0.685	0.64	0.65	0.503	0.204	0.105	0.093	0.050
Max. heat flux ³	1.83	1.68	1.73	1.115	0.583	2.37	1.68	1.15

^{1a} pressurized water reactor; ^{1b} boiling water reactor; ^{1c} high-temperature gas-cooled reactor; ^{1d} liquid metal fast breeder reactor; ^{1e} gas-cooled fast breeder reactor; ^{1f} Canadian pressurized heavy water reactor.

^{2a} Westinghouse; ^{2b} Babcock & Wilcox; ^{2c} General Electric.

³ [MW/m²].

Coolant is under a forced convection flow regime to maximize heat transfer and safety during operation. In addition, some designs allow for a phase change of the coolant to increase heat transfer rates.

Mirrors used for the concentration for high-power laser light experience significant heating. Light beam quality experiences a sharp decline when the mirror begins to distort due to heating [23,24]. To mitigate these negative thermal effects, active cooling of the mirror with water is applied. Table 7 below outlines the assumptions made for simulation regarding the heat transfer area facing the fluid and Figure 8 shows the proposed design. It was found that a microchannel heat sink was able to decrease the thermal deformation of the mirror. Similar to the VLSI circuit heat sink, the microchannels were found to have a high depth to width ratio.

Table 13. Assumed conditions for simulation of a laser disk mirror [23].

Assumed Conditions	Value	Unit
heat flux density	2	MW/m ²
cooling region radius	23.5	mm
mirror thickness	2	mm
channel width	1	mm
channel depth	2	mm
fin width	1.5	mm
water flow rate	500	ml/min
specific mass flow rate	4.8	kg/(m ² ·s)

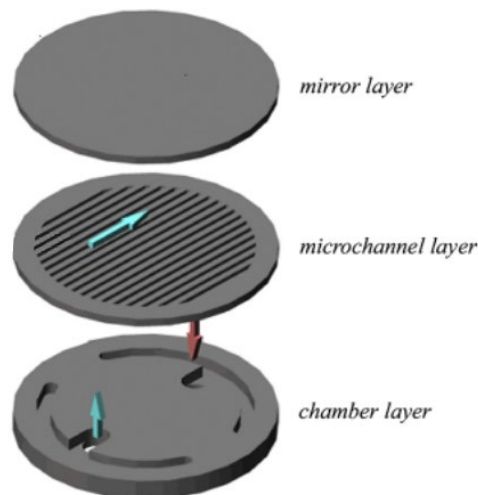


Figure 22: Proposed heat sink for the cooling of a laser mirror [23].

Another high-power heat sink application was designed to limit the temperature rise used in HVDC (high voltage direct current) thyristors in electrical grids. The heat flux associated with the use of this equipment could experience 2 MW/m², under the condition of a very low acceptable temperature increase. The design of the heat transfer surface in this application is also of interest to us. Figure 9 below shows a double layer cross flow matrix of channels that is used to move heat away from the contact surface and limit the temperature rise of a thyristor [25].

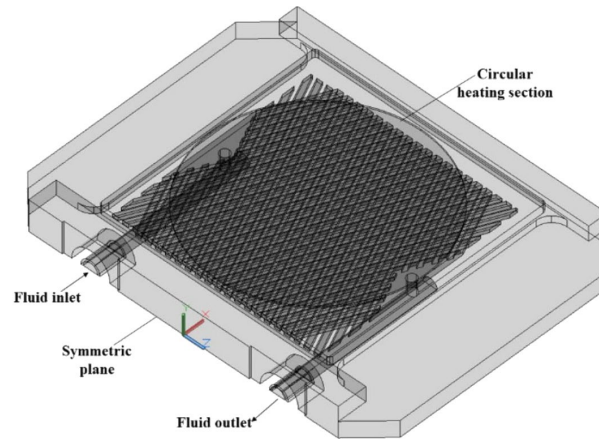


Figure 23: HVDC thyristor heat sink [25].

This design proposes a second example of using small channels near the surface for the purpose of moving large amounts of heat efficiently away from the surface needing to be cooled.

3.2. Design approach

The results of the literature review gave a deeper insight to general design characteristic of high-power heat exchangers tasked with cooling a surface or device. Three of the four designs studied employ the use of small channels to guide coolant near a surface to remove heat. In combination with required geometry of the proposed ARC reactor design the following concept was developed followed by an evaluation with numerical simulation.

3.2.1. Proposed ARC PEXS design

The proposed design provided from literature was used as a starting point for the ARC PEXS [4]. Theoretical principles and designs from other high power heat exchange applications were used to develop a concept for a PEX capable of transferring heat away from the vacuum vessel per the stated boundary conditions. Figure 10 below shows a simplified schematic (a) and illustration (b) of how heat is removed from the fusion reactor.

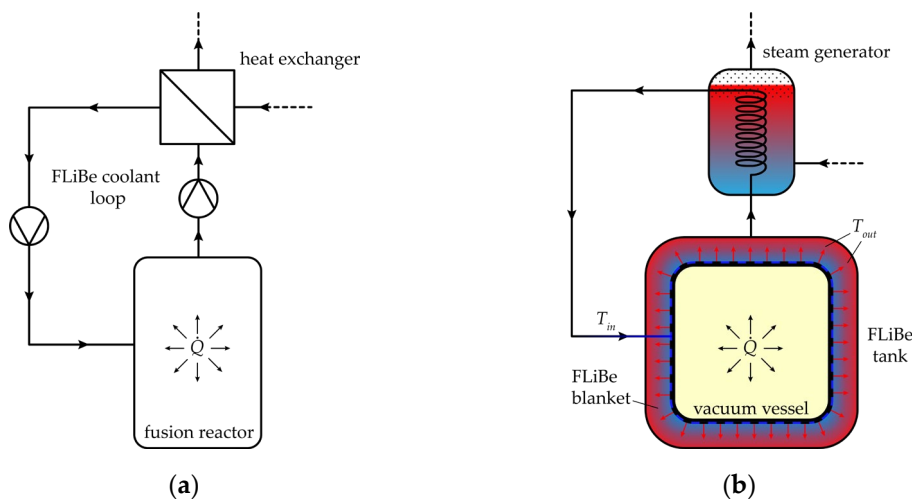


Figure 24: (a) Simple schematic of PEX in operation; (b) Detailed illustration of PEX cooling the vacuum vessel.

FLiBe is circulated over the surface of the fusion reactor (vacuum vessel) to remove heat from the core and transfer heat to a secondary loop (a). Coolant is pumped from the point labeled T_{in} and distributed evenly over the surface of the vacuum vessel (dark blue/black dashed line). It removes heat (\dot{Q}) from the reactor core and maintains operating temperatures below 1500 K on the plasma facing side of the tungsten shell. The heated coolant is discharged locally (red arrows) into the FLiBe tank which encloses vacuum vessel. The heated FLiBe is taken from the tank to generate steam for electricity generation (b). The ARC reactor components relevant for this study are the divertor leg (2), FLiBe blanket (5), and vacuum vessel (8) shown in Figure 11 below.

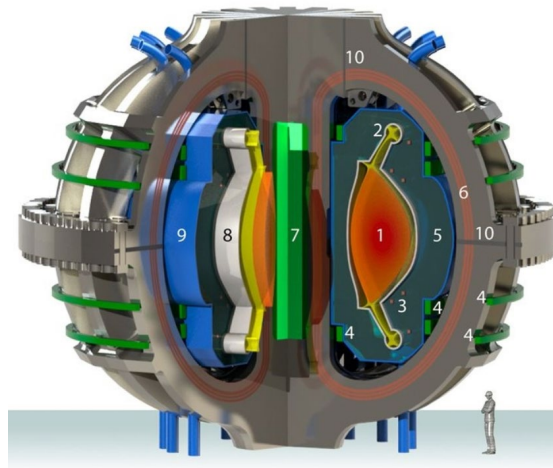


Figure 25: Conceptual design of the ARC reactor [26].

A network of channels supplying coolant to the surface of the vacuum vessel is essential to maintain its structural integrity. Multiple inlets would be necessary to maintain a low temperature change of the coolant while reducing the pressure drop between pump and outlet to the FLiBe blanket. Figure 12 below shows a concept for cooling the divertor leg via a primary supply channel (circular blue pipe) branching into secondary capillary channels (blue longitudinal conduits) before entering a series of finned structures (gray lattice layer) attached to the vacuum vessel.

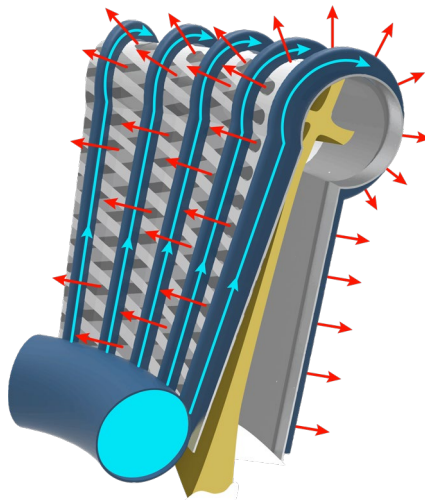


Figure 26: Conceptual design for the PEXS on the divertor leg.

3.2.2. Fluid surface

The construction assumed each fin is attached to an upper cross-fin as shown in Figure 1 at a 90° angle contrary to the geometry in Figure 1. This was chosen to simplify manufacturing and assembly. Consequently, it presents an undesired thermal bridge to the upper channels. Thermal bridging was limited by attaching every other lower channel fin with an upper channel fin resulting in a “ \cap -type” of lower channel geometry. Figure 13 below shows a cross-section (a) and perspective (b) of the \cap -type lower channel.

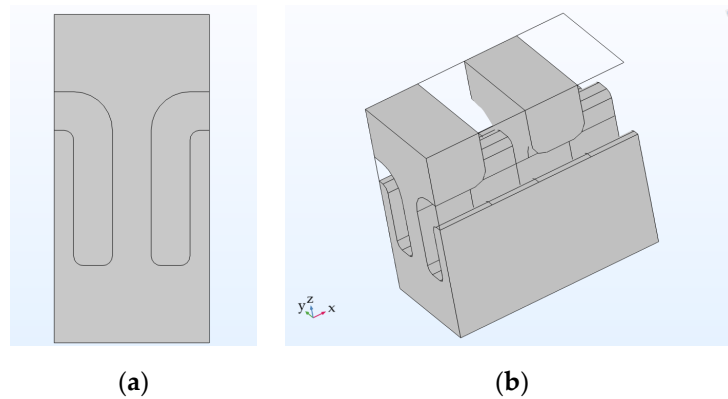


Figure 27: (a) Cross-section of \cap -type lower channel; (b) Perspective of \cap -type lower channel.

3.3. Numerical Simulation

The construction shown in Figure 14 was chosen to take advantage of symmetry planes along xz-planar vertical faces and the right-hand yz-planar vertical face. Figure 14 shows the fluid flow regime as simulated for all cases outlined in Table 3.

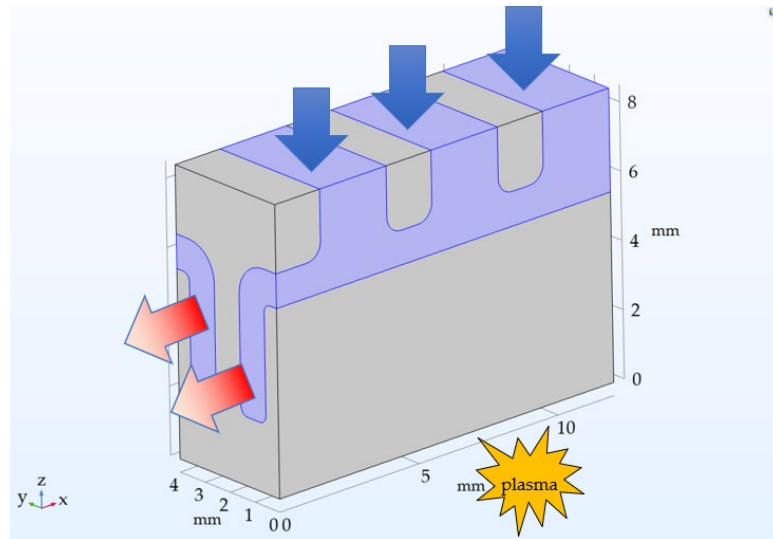


Figure 28: Flow regime as set-up in COMSOL Multiphysics.

Inlets are defined by blue arrows and the outlets by red. Heat from the fusion reaction is applied on the bottom side and enters the fluid stream along the various surfaces of the channels. The illustration above is a rendering of the design concept with three channels in the simulated environment. Geometries with 1, 2, 3, 4, 5, 10, and 20 inlets for each fin length

were analyzed for a total of 18 unique assessments. Figure 15 below shows a 20-inlet geometry.

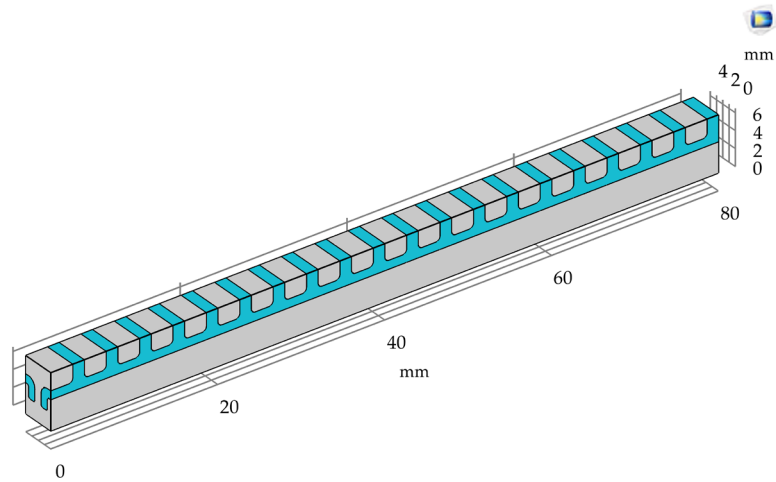


Figure 29: Example of a 20-inlet geometry.

Each combination of parameters was using a mass flow rate consistent with the area specific mass flow rate calculated in section 2.2.1.

Thermal performance was first assessed by analyzing the average outlet temperature of each configuration. Figure 16 below shows calculated average outlet temperatures for each fin length (1.5, 2.5, and 3.5 mm) shown in the legend.

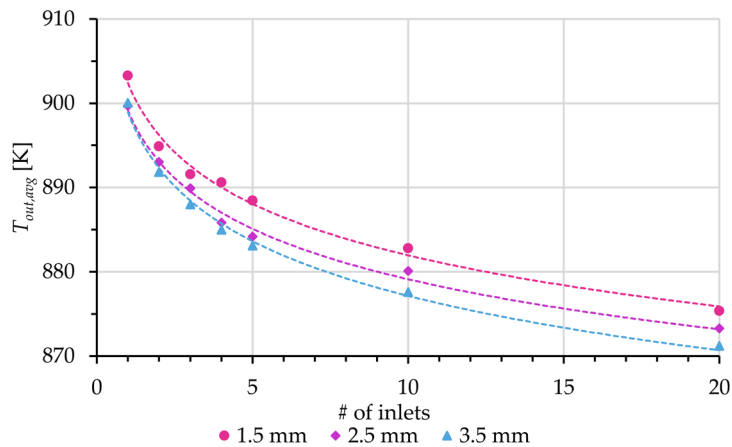


Figure 30: Average outlet temperatures for each simulated geometry

Each successive addition of inlets showed a reduction in average fluid temperature at the outlet. This was expected as the addition of inlets introduced more FLiBe to a channel with fixed cross-sectional area. Maximum fluid velocity (u_{max}), increased with the number of inlets while decreasing with fin length (f_L) for geometries with the same number of inlets. The maximum domain temperature, (T_{max}), and average heat transfer coefficient on the fluid surface, ($\bar{\alpha}_f$), also decreased with the addition of inlets up to 3-4 inlets before increasing again. The maximum pressure-drop from inlet to outlet across each geometry, (Δp_{max}), increased with increasing u_{max} . Table 8 below shows the trends observed organized by fin length, area ratio, and average minimum heat transfer coefficient, (α_{min}), for each geometry by the number of inlets (N_{in}).

Table 14. Estimated electrical power consumption with increasing PEXS pressure losses.

f_L [mm]/ A_r [-]; α_{min}^3 [W/(m · K)]	N_{in} [-]	u_{max}^1 [m/s]	T_{max}^1 [K]	$\bar{\alpha}_f^1$ [W/(m · K)]	Δp_{max}^1 [Pa]	P_{el}^{2*} [MW]
1.5/2.5; 9160	1	0.134	1465	10703	39	14.4
	2	0.260	1433	11222	133	14.4
	3	0.393	1429	11266	269	13.3
	4	0.527	1434	10842	443	12.2
	5	0.666	1434	10851	675	11.8
	10	1.350	1556	8542	2774	9.6
	20	2.664	1917	8472	8494	8.0
2.5/3.5; 6540	1	0.102	1467	9324	27	11.1
	2	0.199	1435	10146	82	10.6
	3	0.300	1435	9927	162	8.0
	4	0.402	1425	10118	285	7.8
	5	0.518	1442	9740	423	7.3
	10	1.033	1621	7340	1569	5.4
	20	2.026	2131	5495	4806	4.2
3.5/4.5; 5090	1	0.081	1486	9510	22	9.3
	2	0.160	1449	9364	59	6.9
	3	0.246	1448	9193	114	5.6
	4	0.328	1464	8922	185	5.0
	5	0.413	1490	8524	273	4.6
	10	0.855	1692	6596	1032	3.6
	20	1.675	2368	4549	3170	2.8

¹ Simulated output.² Calculated with simulated output.³ Calculated with theory section 2.2.1.

* Hydraulic power needed to supply FLiBe to the tungsten vacuum vessel only.

Simulated results indicate thermal performance satisfying boundary conditions for geometries with 1 to 5 inlets based on T_{max} . The minimum average heat transfer coefficient for a 2 mm thick tungsten wall and flat plate (α_{min}) is not consistent with maximum temperature results. Simulated geometries included thermal bridges and a cool side boundary condition not considered in the theoretical analysis. Errors associated with the model, the use of average domain values for calculations (e.g., average outlet temperature), and deviations from theory explain simulations where T_{max} exceeded 1500 K while $\bar{\alpha}_f$ exceed α_{min} .

4. Conclusion

The results of this study have determined there is a viable path forward to develop a PEXS capable of fulfilling the thermodynamic constraints of the ARC reactor design. Theory regarding heat transfer, fin and surface efficiency, and fluid dynamics were used as design guides for the development of a concept analyzed using numerical simulation. Analysis of concept performance indicated positive progress in developing a heat exchange surface capable of transferring a specific heat flux of 12 MW/m². Simulated heat transfer coefficients for the fluid surface approach values found using an energy balance for heat exchangers. The most feasible solution was a channeled block of tungsten with fins of 3.5 mm in height, fin and channel width of 1 mm, and 5 sequential inlets. It represented the solution with the lowest pressure losses and thus only consumes 2.3% of

the produced electrical power generated. However, the simulated results were not fully in agreement with the theory. Further investigation is necessary into the accuracy of the model by means of empirical results and tests in a laboratory setting.

Before moving forward with the proposed geometries, the calculated and simulated numerical results in this work need verification. The construction of an experimental test rig for measuring empirical performance is required to understand the accuracy of calculated and simulated results. A design of experiment must be developed using the materials (or their analogs) which accurately model the problem described in this work.

Author Contributions: Conceptualization, R.B. and L.F.; methodology, R.B. and L.F.; software, R.B.; formal analysis, R.B., L.F.; writing—original draft preparation, R.B.; writing—review and editing, R.B., C.S., and L.F.; All authors have read and agreed to the published version of the manuscript.

Funding: This research received no external funding.

Acknowledgments: The authors would like to thank all involved with developing and supporting this study.

Conflicts of Interest: The authors declare no conflict of interest.

5. References

- [1] EUROfusion, EUROfusion, (2022). <https://www.euro-fusion.org/fusion/history-of-fusion/#c2407> (accessed May 23, 2022).
- [2] A. Eddington, The Internal Constitution of the Stars, *Nature*. 106 (1920) 14–20. <https://doi.org/https://doi.org/10.1038/106014a0>.
- [3] M.L.E. Oliphant, P. Harteck, O.M. Rutherford, Transmutation Effects Observed with Heavy Hydrogen, *Proc. R. Soc.* 144 (1934) 692–703.
- [4] A.Q. Kuang, N.M. Cao, A.J. Creely, C.A. Dennett, J. Hecla, B. LaBomard, R.A. Tinguely, E.A. Tolman, H. Hoffman, M. Major, J. Ruiz Ruiz, D. Brunner, P. Grover, C. Laughman, B.N. Sorbom, D.G. Whyte, Conceptual design study for heat exhaust management in the ARC fusion pilot plant, *Fusion Energy Des.* 137 (2018) 221–242. <https://doi.org/https://doi.org/10.1016/j.fuseng-des.2018.09.007>.
- [5] Tungsten, Midwest Tungsten Serv. (2022). <https://www.tungsten.com/material-info/tungsten-w> (accessed May 23, 2022).
- [6] R. Aldrich, Laser Fundamentals, *Nav. Surf. Warf. Cent.* (n.d.). <https://man.fas.org/dod-101/navy/docs/laser/fundamentals.htm#LASER TYPES> (accessed January 26, 2022).
- [7] L. Hu, B.D. Wirth, D. Maroudas, Thermal conductivity of tungsten: Effects of plasma-related structural defects from molecular-dynamics simulations, *Appl. Phys. Lett.* 111 (2017). <https://doi.org/10.1063/1.4986956>.
- [8] A. Suslova, O. El-Atwani, D. Sagapuram, S.S. Harilal, A. Hassanein, Recrystallization and grain growth induced by ELMs-like transient heat loads in deformed tungsten samples, *Sci. Rep.* 4 (2014) 1–11. <https://doi.org/10.1038/srep06845>.
- [9] P.N. Haubenreich, J.R. Engel, Experience with the Molten-Salt Reactor Experiment, *Nucl. Appl. Technol. Volume 8* (1970) 118–136. <https://doi.org/https://doi.org/10.13182/NT8-2-118>.
- [10] R.W. Moir, HY LIFE-II Inertial Confinement Fusion Reactor Design, *Fusion Technol.* 19 (1991) 617–624. <https://doi.org/https://doi.org/10.13182/FST91-A29414>.
- [11] L.C. Cadwallader, G.R. Longhurst, Flibe Use in Fusion Reactors: an Initial Safety Assessment, *Idaho Natl. Eng. Environ. Lab.* (1999) 1–25. <https://www.osti.gov/servlets/purl/752080>.
- [12] R.R. Romatoski, L.W. Hu, Fluoride salt coolant properties for nuclear reactor applications: A review, *Ann. Nucl. Energy.* 109 (2017) 635–647. <https://doi.org/10.1016/j.anucene.2017.05.036>.
- [13] Inconel 718 Technical Data, *High Temp. Met.* (2015). <https://www.hightempmet-als.com/techdata/hitempInconel718data.php> (accessed January 27, 2022).
- [14] R. Cortés, E.R. Barragán, V.H. López, R.R. Ambriz, D. Jaramillo, Mechanical properties of Inconel 718 welds performed by gas tungsten arc welding, *Int. J. Adv. Manuf. Technol.* 94 (2018) 3949–3961. <https://doi.org/10.1007/s00170-017-1128-x>.
- [15] COLE NC, GILLILAND RG, SLAUGHTER GM, Weldability of tungsten and its alloys, *Weld J.* 50 (1971).

- [16] M. Kind, H. Martin, Verein Deutscher Ingenieure (VDI) - Heat Atlas, Springer Heidelberg Dordrecht London New York, 2010.
- [17] T.L. Bergman, A.S. Lavine, F.P. Incropera, D.P. DeWitt, Fundamentals of Heat and Mass Transfer, 7th Editio, John Wiley & Sons, 2011.
- [18] B.N. Sorbom, J. Ball, T.R. Palmer, F.J. Mangiarotti, J.M. Sierchio, P. Bonoli, C. Kasten, D.A. Sutherland, H.S. Barnard, C.B. Haakonsen, J. Goh, C. Sung, D.G. Whyte, ARC: A compact, high-field, fusion nuclear science facility and demonstration power plant with demountable magnets, Fusion Eng. Des. 100 (2015) 378–405. <https://doi.org/10.1016/j.fusengdes.2015.07.008>.
- [19] COMSOL, COMSOL Multiphysics®, (2022). <https://doc.comsol.com/6.0/docserver/#!/com.comsol.help.comsol/helpdesk/helpdesk.html> (accessed July 20, 2022).
- [20] W.A. Scott, Cooling of electronic equipment, John Wiley & Sons, New York, 1974.
- [21] D.B. Tuckerman, R.F.W. Pease, High-Performance Heat Sinking for VLSI, IEEE Electron Device Lett. EDL-2 (1981) 126–129. <https://doi.org/10.1109/EDL.1981.25367>.
- [22] J.J. Duderstadt, L.J. Hamilton, Nuclear Reactor Analysis, (1976) 675.
- [23] H. Cao, G. Chen, Optimization design of microchannel heat sink geometry for high power laser mirror, Appl. Therm. Eng. 30 (2010) 1644–1651. <https://doi.org/10.1016/j.applthermaleng.2010.03.022>.
- [24] Y.F. Peng, Z.H. Cheng, Y.N. Zhang, J.L. Qiu, Laser-induced temperature distributions and thermal deformations in sapphire, silicon, and calcium fluoride substrates at 1.315 μm , Opt. Eng. 40 (2001) 2822. <https://doi.org/10.1117/1.1418712>.
- [25] Q. Li, L. Fischer, G. Qiao, E. Mura, C. Li, Y. Ding, High performance cooling of a HVDC converter using a fatty acid ester-based phase change dispersion in a heat sink with double-layer oblique-crossed ribs, Int. J. Energy Res. 44 (2020) 5819–5840. <https://doi.org/10.1002/er.5347>.
- [26] D. Chandler, A new path to solving a longstanding fusion challenge., MIT News. (2018). <https://news.mit.edu/2018/solving-excess-heat-fusion-power-plants-1009> (accessed February 13, 2022).

5 References

- [1] A.Q. Kuang, N.M. Cao, A.J. Creely, C.A. Dennett, J. Hecla, B. LaBomard, R.A. Tinguely, E.A. Tolman, H. Hoffman, M. Major, J. Ruiz Ruiz, D. Brunner, P. Grover, C. Laughman, B.N. Sorbom, D.G. Whyte, Conceptual design study for heat exhaust management in the ARC fusion pilot plant, *Fusion Energy Des.* 137 (2018) 221–242. <https://doi.org/https://doi.org/10.1016/j.fusengdes.2018.09.007>.
- [2] CFS, Designing and building fusion energy systems to power the world, (2022). <https://cfs.energy/technology> (accessed January 4, 2023).
- [3] Hyme Energy ApS, New Molten Salt Storage for the Energy Transition, (2022). <https://www.hyme.energy/technology> (accessed January 4, 2023).
- [4] Seaborg, Rethinking Nuclear, (2022). <https://www.seaborg.com/the-reactor> (accessed January 4, 2023).
- [5] MAN Energy Solutions, High-quality salt-operated tubular reactors from DWE®, (2022). <https://www.man-es.com/process-industry/products/chemical-reactors/salt-operated-reactors> (accessed January 4, 2023).
- [6] ORNL, Nuclear Energy and Fuel Cycle Division: Molten Salt Reactor, (2022). <https://www.ornl.gov/molten-salt-reactor> (accessed January 4, 2023).
- [7] D.F. Williams, L.M. Toth, K.T. Clarno, Assessment of Candidate Molten Salt Coolants for the Advanced High-Temperature Reactor (AHTR), 2006. [5] of molten salt.
- [8] M. Kind, H. Martin, Verein Deutscher Ingenieure (VDI) - Heat Atlas, Springer Heidelberg Dordrecht London New York, 2010.
- [9] KNF, FP 1.400 membran flüssigkeitspumpen, (2023) 1–3. www.knf.com.
- [10] SMC Corporation, Drosselrückschlagventil mit Steckverbindung, Tokyo, Japan, 2023.
- [11] C.B. Gmbh, C. Kg, Typ 8077 Ovalrad Durchflusssensor für kleine Durch - flussmengen Inhaltsverzeichnis, (2019) 1–8.
- [12] M. Probst, Heiz Patronen, Niederbuchsiten, Switzerland, 2022.
- [13] A.F. Armaflex, AF/ArmaFlex ®, Münster, Germany, 2023. <https://local.armacell.com/fileadmin/cms/uk/products/en/AFArmaFlexClassORangeUKROI.pdf>.
- [14] Deutsches Kupferinstitut, Cu-ETP, Düsseldorf, 2005. <https://kupfer.de/>.
- [15] TC Direct, TC Direct, (2023). <https://www.tcdirect.co.uk/product-2-230-29/Miniature-RTD-Sensor-Pt100-0-5-to-1-6mm-diameter> (accessed January 11, 2023).
- [16] Dielectric Manufacturing, Teflon® (Polytetrafluoroethylene, PTFE), (2023). <https://dielectricmfg.com/knowledge-base/teflon/> (accessed January 11, 2023).

- [17] Laminated Plastics, Technical Data Sheet Teflon (PFTE), (2023).
<https://laminatedplastics.com/teflon.pdf> (accessed January 11, 2023).
- [18] RS Pro, PFTE, (2023). <https://docs.rs-online.com/bac9/0900766b81677682.pdf> (accessed January 11, 2023).